

Gravitational Lensing by Ring-Like Structures

Ethan Lake¹^{*} and Zheng Zheng¹[†]

¹*Department of Physics and Astronomy, University of Utah, 115 South 1400 East, Salt Lake City, UT 84112, USA*

8 November 2021

ABSTRACT

We study a class of gravitational lensing systems consisting of an inclined ring/belt, with and without an added point mass at the centre. We show that a common property of such systems is the so-called “pseudo-caustic”, across which the magnification of a point source changes discontinuously and yet remains finite. Such a magnification change can be associated with either a change in image multiplicity or a sudden change in the size of one of the images. The existence of pseudo-caustics and the complex interplay between them and the formal caustics (corresponding to points of infinite magnification) can lead to interesting consequences, such as truncated or open caustics and the violation of Burke’s theorem. The origin of the pseudo-caustics is found to be the discontinuity in the solutions to the lens equation across the ring/belt boundaries, and the pseudo-caustics correspond to these boundaries in the image (lens) plane. We provide a few illustrative examples to understand the pseudo-caustic features, and in a separate paper we consider a specific astronomical application of microlensing by extrasolar asteroid belts.

Key words: gravitational lensing: strong — gravitational lensing: micro — asteroids: general

1 INTRODUCTION

Gravitational lensing has developed from an interesting novelty predicted by general relativity (Einstein 1936) to an essential tool in modern astrophysics. It has been applied with great success to (among other things) detect extrasolar planets (e.g., Mao & Paczynski 1991; Bond et al. 2004; Batista et al. 2014), estimate the masses of galaxy clusters (e.g., Tyson et al. 1998; Bradač et al. 2009; Hoekstra et al. 2013), and determine the large-scale distribution of matter in the Universe (e.g., Wittman et al. 2000; Vikram et al. 2015). In addition, the theoretical study of gravitational lensing systems is of interest in mathematics, namely in catastrophe theory and Morse theory (e.g., Erdl & Schneider 1993; Petters 1995; Petters et al. 2001).

One common goal of examining lensing systems from a theoretical standpoint is the characterization of the magnification of a source at a given position from the lens mapping. In particular, there exist singularities in the mapping which form caustic curves in the source plane where the magnification is formally infinite. Studying the behaviour of these curves allows for the determination of certain properties of the lens mapping, and provides information about the number of images a source generates. Normally the number of images of a source changes when, and only when, the source crosses a caustic curve. However, some lens models have been found to violate this principle, namely singular isothermal spheres and ellipsoids (e.g., Kovner 1987; Evans & Wilkinson 1998; Rhie 2010) and variants thereof (Wang & Turner 1997; Shin

& Evans 2008; Tessore & Metcalf 2015). These systems possess features called “pseudo-caustics”, where the number of images of a source changes without the source crossing a caustic.

In this paper, we examine lensing systems consisting of a circular ring/belt at various inclinations, with or without a point mass at the centre. We find that these systems possess more general types of pseudo-caustics, characterized by a discontinuous but finite change in magnification. They are either associated with a change in image multiplicity or with a sudden change in the size of an image. These pseudo-caustics produce complex and interesting magnification patterns, despite the relative simplicity of the lensing system. We aim to obtain a basic understanding of such lensing systems.

Although our interest here is mainly theoretical and phenomenological, such kind of lensing systems exist in astronomy, like the asteroid belt around a star. In a related paper (Lake, Zheng, & Dong 2015), aided by the results presented here, we study the microlensing signatures of extrasolar asteroid belts and explore the possibility of detection with future surveys.

This paper is organized as follows. In Section 2, we briefly recall key gravitational lens equations and present the solutions to the lensing systems we consider. In Section 3, we examine the magnification patterns and pseudo-caustic structures for each of the systems in consideration. We summarize our results and discuss implications in Section 4.

^{*} Contact e-mail: lake@physics.utah.edu

[†] Contact e-mail: zhengzheng@astro.utah.edu

2 SOLUTIONS TO THE LENS EQUATION

In all the geometries we consider in this paper, a background source is lensed by a mass lying between the source and the observer. We denote the angular position in the image and source plane as $\mathbf{r}_I = (x_I, y_I)$ and $\mathbf{r}_S = (x_S, y_S)$, respectively. They are put in units of the Einstein ring radius,

$$\theta_E = \sqrt{\frac{4GM}{c^2} \frac{D_{LS}}{D_L D_S}}, \quad (1)$$

where D_L , D_S , and D_{LS} are the (angular diameter) distances between the observer and the lens, the observer and the source, and the lens and the source, respectively. The mass M is the total mass of the lens system we consider.

The general lens equation can be written as

$$\mathbf{r}_S = \mathbf{r}_I - \alpha(\mathbf{r}_I). \quad (2)$$

The normalized deflection angle α is found by integrating the contribution over the projected mass distribution of the lens,

$$\alpha(\mathbf{r}_I) = \frac{1}{\pi} \int d^2 r'_I \kappa(\mathbf{r}'_I) \frac{\mathbf{r}_I - \mathbf{r}'_I}{|\mathbf{r}_I - \mathbf{r}'_I|^2}, \quad (3)$$

where $\kappa(\mathbf{r}_I)$ is the dimensionless projected surface mass density of the lens,

$$\kappa(\mathbf{r}_I) = \frac{\Sigma(\mathbf{r}_I)}{\Sigma_{\text{cr}}}. \quad (4)$$

The critical surface density Σ_{cr} is defined as

$$\Sigma_{\text{cr}} \equiv \frac{c^2 D_S}{4\pi G D_L D_{LS}}. \quad (5)$$

For a circularly symmetric lens, Σ_{cr} is equal to the mean surface density inside the Einstein ring radius.

The magnification of the image at \mathbf{r}_I can be computed as

$$\mu(\mathbf{r}_I) = \frac{1}{\det(A)}, \quad (6)$$

where $\det(A)$ is the determinant of the lensing Jacobian A_{ij} , formed from the derivatives of the lensing deflection $\alpha = \alpha_x \hat{x} + \alpha_y \hat{y}$,

$$A_{ij} = \delta_{ij} - \frac{\partial \alpha_i}{\partial x_j}, \quad (7)$$

with $x_1 = x$ and $x_2 = y$. The total magnification for multiple images is obtained by $\sum_i |\mu_i|$, where i runs over all images.

For the investigation in this paper, we derive the lens equation for a lensing system composed of a thin circular belt with or without a point mass at the centre. We first show the face-on case to build an intuitive understanding and then generalize to inclined belts. For simplicity, we assume the belt to have a uniform surface density. We choose the centre of the belt in projection as the origin, and in the case of the inclined belt, the directions of the major and minor axis as \hat{x} and \hat{y} .

2.1 Face-on Systems

As a first step, we consider a uniform thin circular belt seen face-on, centred at the origin, with radius a (in units of the Einstein ring radius). This lensing geometry has been briefly studied before (Schneider et al. 1992, p.247), and here we present a more detailed analysis.

We start by considering lensing by a face-on ring (a belt with zero width). Rays passing outside the ring ($r_I > a$) experience a deflection as if the ring were a point mass located at the origin,

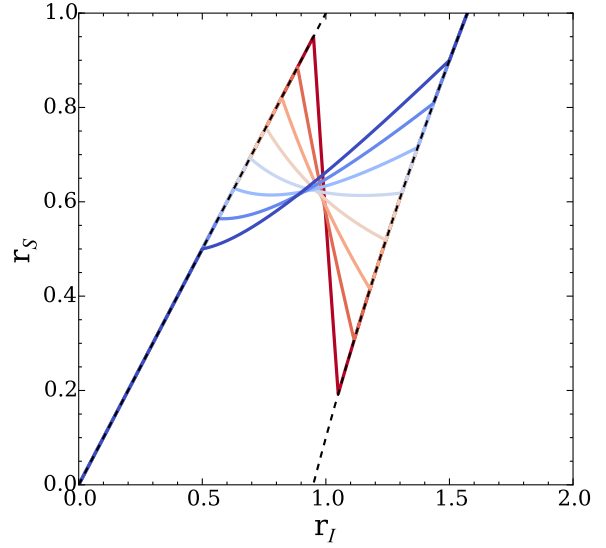


Figure 1. Solutions to the lens equation for a face-on belt with different widths. All belts have equal mass and each has a mean radius of 1 (in units of the Einstein ring radius). The left and right dashed curves correspond to undeflected rays and rays that are deflected by the belt acting as a point mass, respectively. The solid curves show the allowed solutions, with the width of the belt increasing from red to blue. Note that in the limit of an infinitesimally thin ring the downward-sloping section disappears (or becomes vertical) and the corresponding image vanishes (as it becomes zero-sized).

while rays passing through the ring ($r_I < a$) are undeflected. The latter result can be easily inferred by considering two chords passing through the impact point with an infinitesimally small opening angle between them – the deflection angles caused by the two arc elements on the ring bounded by the two chords are the same but in the opposite directions, leading to null contribution to the deflection.

The generalization from a thin ring to a belt is straightforward. Only the mass inside the circle intersecting the impact point contributes to the deflection, as if it were a point mass at the centre. For a belt of constant surface density with inner and outer radii a_i and a_o , we have

$$\mathbf{r}_S = \mathbf{r}_I - \frac{1}{r_I} R \left(\frac{r_I^2 - a_i^2}{a_o^2 - a_i^2} \right), \quad (8)$$

where $R(x)$ is a modified ramp function defined as

$$R(x) = \begin{cases} 0 & \text{if } x \leq 0, \\ x & \text{if } 0 < x \leq 1, \\ 1 & \text{if } x > 1. \end{cases} \quad (9)$$

The solution to equation (8) is plotted in Figure 1 for a fixed belt mass with different values of the belt width $\Delta a = a_o - a_i$. With a mean radius $a = (a_i + a_o)/2 = 1$, the belt has width extending up to $\Delta a = 1$. The left dashed line corresponds to undeflected rays, which is the solution for rays passing interior to the inner edge of the belt ($r_I < a_i$). The right dashed curve is the solution for rays deflected by the whole belt (equivalent to putting all the mass of the belt at the origin), which is the solution for rays passing exterior to the outer edge of the belt. We refer to the two types of solutions as the interior and exterior solution, respectively. For rays passing through the belt, if the belt is wide (low surface density),

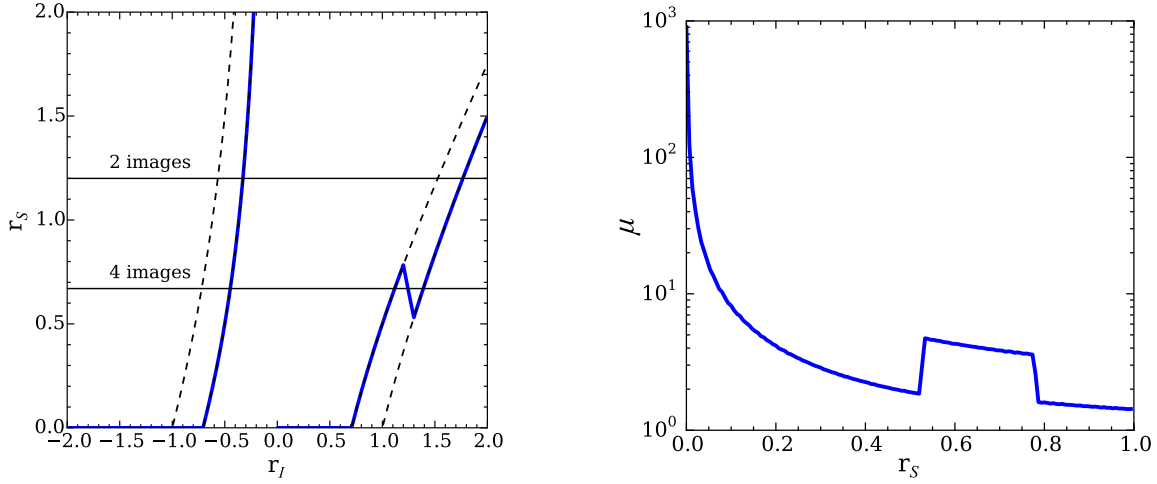


Figure 2. *Left:* Solutions to the lens equation for a belt+point lens. The belt is face-on, with mean radius $a = 1.25$ and width $\Delta a = 0.1$. The belt to point mass ratio is set to $q = 1.0$. The two inner (outer) smooth curves correspond to the solutions from just point mass (from the total belt+point mass system acting as a point mass). The solid curves are the allowed solutions for the belt+point case. The presence of the belt creates a region in the source plane that correspond to four images. *Right:* Magnification for the lens in the left plot as a function of the distance of the point source from the origin. The step-like jump in magnification marks the pseudo-caustics (see the text), and the plateau bounded by the two steps corresponds to source positions where four images are formed.

r_s increases as r_l increases. However, if the belt is narrow (high surface density), r_s decreases as r_l increases. The reason is that as r_l increases, the high surface density makes a substantial increase in the mass inside the radius of the impact point, which causes a large deflection and allows rays from small r_s to be deflected to the observer. The interior and exterior solutions are joined by rays passing through the belt, which complete the final solution.

In Figure 1, the number of images formed by a point source at a radius of r_s in the source plane is found by counting the number of intersection points of the solution curve with a horizontal line at r_s . For wide belts with low surface density, only one image is formed. For thinner belts with high surface densities, up to three images can be formed. In the limit of the thin ring, the central image disappears, since its size is zero even for a source of finite size. The remaining two images correspond to undeflected rays passing inside the ring and rays passing outside the ring that are then deflected to the observer.

Based on the solution of the belt-only case, we see that if a source moves from the origin to large radii in the source plane, the total magnification changes discontinuously as the images (or impact points) cross the belt. The change is caused either by the corresponding change in the number of images for a narrow belt, or by the change in the image size (i.e., change in the r_s-r_l mapping) for a wide belt. The loci in the source plane associated with the discontinuous change in magnification are defined as pseudo-caustics.

We now introduce a point mass to our lensing system, located at the centre of the face-on belt. We denote the mass ratio of the belt to the point mass as q and normalize the angular positions by the the Einstein ring radius for the combined belt+point system. This has the effect of adding an extra term (the lensing contribution from the point mass) to the lens equation, with equation (8) becoming

$$r_s = r_l - \frac{1}{1+q} \frac{1}{r_l} - \frac{q}{1+q} \frac{1}{r_l} R \left(\frac{r_l^2 - a_i^2}{a_o^2 - a_i^2} \right). \quad (10)$$

The solution to this equation is plotted in the left panel of Fig-

ure 2 for a face-on belt with $a_i = 1.2$, $a_o = 1.3$, and $q = 1$. Negative values of r_l correspond to images with negative parity (i.e., images located on the opposite side of the point mass as the source).

The two middle curves (with the left one masked in solid, and the right one half masked in solid) correspond to the possible solutions to the lensing equation for rays passing interior to the belt, where only the central point mass is responsible for the deflection. The two dashed curves at large $|r_l|$ are the possible solutions for rays passing exterior to the belt, where the deflection comes from the total mass of the system. The solutions include cases with both positive and negative parity. Although the far left dashed curve is supposed to include rays deflected from both the belt and the point mass, the rays in fact pass interior to the belt (i.e., $|r_l| < a_i$), meaning that this solution is not physically realized. The middle right dashed curve corresponds to rays passing interior to the belt and deflected only by the point mass. For $r_l > a_i$, deflection from the belt starts to contribute and this solution is not allowed. Similarly, for the rightmost dashed curve, the allowed solution should have an image position beyond the outer radius of the belt, i.e., $r_l > a_o$. As a whole, the solid curves represent the physically realized solution. The transition from the interior solution to the exterior solution is that with the impact points within the range of the belt ($a_i < r_l < a_o$). Since the belt is narrow (high surface density), r_s decreases with increasing r_l in this part of the solution (see Figure 1 for a comparison).

The right panel of Figure 2 shows the total magnification a point source experiences when lensed by the face-on belt+point system, as a function of distance from the origin in the source plane. At both small r_s and large r_s , the source has two images (see the left panel of Figure 2), while at r_s around 0.55–0.75, the source has four images. In the magnification map, as the number of images changes from two to four, there is a sharp increase in the magnification (about a factor of 2.5). Note that the source does not need to cross a caustic (defined as the locus in the source plane with infinite magnification for a point source) for the number of images to change. The associated loci across which the magnification is finite

but changes discontinuously are pseudo-caustics. The existence of pseudo-caustics implies that we cannot rely solely on the formal caustics in order to understand these lensing systems.

2.2 Inclined Systems

We now allow our system to be inclined, with the belt normal direction at an angle i relative to the line of sight. We again start with the case of a uniform ring with radius a , which becomes an ellipse when seen in projection. The ellipse is parametrized by the equation

$$\frac{x^2}{a^2} + \frac{y^2}{b^2} = 1, \quad (11)$$

where a is the semi-major axis and $b = a \cos i$ is the semi-minor axis. Even for arbitrary inclinations, rays passing interior to the ring are remarkably still undeflected (Chandrasekhar 1969; Bray 1984). To find the deflection for an impact point \mathbf{r}_I that lies outside the ring (i.e., the exterior solution), we consider an ellipse passing through \mathbf{r}_I and confocal to the projected ring. The confocal ellipse is parametrized by the equation

$$\frac{x^2}{a'^2} + \frac{y^2}{b'^2} = 1, \quad (12)$$

where the primed semi-axes are defined by $a'^2 = a^2 + \lambda$ and $b'^2 = b^2 + \lambda$, with λ found by substituting $\mathbf{r}_I = (x_I, y_I)$ into equation (12).

The deflection angle $\alpha(\mathbf{r}_I) = \alpha_1 \hat{\mathbf{x}}_I + \alpha_2 \hat{\mathbf{y}}_I$ from the ring can be found analytically using results from ellipsoidal potential theory (Bourassa & Kantowski 1975), which are solved nicely in Schramm (1990). The deflection angle is

$$\alpha(\mathbf{r}_I) = -p'^2 \left(\frac{x_I}{a'^3 b'} + \frac{y_I}{a' b'^3} \right), \quad (13)$$

where $p' = \left(x_I^2/a'^4 + y_I^2/b'^4 \right)^{-1/2}$ is the perpendicular distance from the centre of the confocal ellipse to the tangent line at \mathbf{r}_I .

To obtain an expression for the deflection caused by a belt, we make use of more results in ellipsoidal potential theory. Consider a circular uniform disc in projection, which appears as an elliptical disc with constant normalized surface density κ_0 and semi-axes a and b . The normalized deflection angle at a point \mathbf{r}_I exterior to the disc is (Schramm 1990)

$$\alpha(\mathbf{r}_I) = -2\pi ab\kappa_0 \left(\frac{1}{a' + b'} \frac{x_I}{a'} + \frac{1}{a' + b'} \frac{y_I}{b'} \right), \quad (14)$$

with a' and b' retaining their meanings from equation (12). For a point interior to the disc, we simply set $\lambda = 0$ so that $a' = a$ and $b' = b$. To calculate the deflection angle of a belt of inner and outer semi-major axes a_i and a_o , we can superimpose a disc with semi-axes a_o and b_o and surface density κ_0 with a disc of negative surface density $-\kappa_0$ and semi-axes a_i and b_i . The total deflection $\alpha(\mathbf{r}_I)$ from the two superimposed discs is just that from a uniform belt with inner and outer radii a_i and a_o . Note that here κ_0 is defined as $\kappa_0 = 1/[\pi(a_o b_o - a_i b_i)]$ for the belt so that the total dimensionless mass is unity.

With the deflection angle $\alpha(\mathbf{r}_I)$ from the belt, the lens equation for the general case of an inclined belt+point system then becomes

$$\mathbf{r}_S = \mathbf{r}_I - \frac{1}{1+q} \frac{1}{r_I^2} \mathbf{r}_I - \frac{q}{1+q} \alpha(\mathbf{r}_I), \quad (15)$$

where q is the belt-to-point mass ratio. The second term on the right-hand side corresponds to the deflection from the centre point

mass. Taking the limit of $q \rightarrow +\infty$ gives the equation for the belt-only case.

Equipped with the solutions of the deflection angle and the lens equation for the inclined system and using our understanding of the face-on system, we turn now to investigate the general lensing properties of belt+point mass system as a function of the inclination.

3 LENSING PROPERTIES OF BELT+POINT SYSTEMS: CAUSTICS AND PSEUDO-CAUSTICS

To study the lensing properties of belt+point lensing systems, we employ the inverse ray-shooting technique (e.g., Schneider & Weiss 1986). Light rays are drawn uniformly from the image plane and mapped back to the source plane according to the lens equation. The magnification at each position in the source plane is computed as the ratio of the density of rays at this position to that in the image plane (which is also the density of rays in the source plane in the absence of the lens).

Of interest in analysing the properties of lensing systems is the behaviour of caustic curves, which are loci in the source plane with singular Jacobian matrix ($\det(A) = 0$) of the lens mapping (i.e., where the magnification μ is formally infinite). For all but the most simple lensing geometries, finding analytical expressions for the caustic curves is difficult, since the mapping $\mathbf{r}_I \mapsto \mathbf{r}_S$ is highly non-linear. While the inverse-ray shooting technique enables us to find high magnification regions, it is limited by the resolution of the mapping. To better locate the caustic curves, we use equation (6) to track down points where the magnification is above some threshold value (we adopt $|\mu| > 1000$). In the Appendix, we provide analytic expressions of magnification for ring/belt+point lens systems.

For normal lensing systems, the number of images of a source changes when (and only when) the source crosses a caustic (Schneider et al. 1992). This is because the lens mapping is normally continuous away from the caustic set, and since the connectedness of a set is preserved under a continuous mapping, image changes can only occur at caustics. Additionally, the image multiplicity must change by two for any caustic crossing, and the total number of images is always odd (Burke 1981; McKenzie 1985). These restrictions on image formation (known as Burke's Theorem) necessitate that the caustic set forms closed curves. If there were open caustics with finite extent, a closed loop could be constructed in the source plane that had only one intersection with a caustic. A source traveling along this loop would then arrive back at its starting point with a different image multiplicity than it started with, which is impossible.

The lenses we consider in this paper are interesting exceptions. As is already shown in the face-on belt case and will be studied in detail below, there exist regions in the source plane dubbed ‘‘pseudo-caustics’’, across which the magnification changes discontinuously even though $\det(A) \neq 0$, and where the invariance of the image parity is violated. The pseudo-caustics are found to possess a broad variety of morphologies across the parameter space of the lensing system considered here. In many cases, we will see that the existence of pseudo-caustics can lead to open caustics. Several studies have dealt with pseudo-caustics, all in the study of variants of singular isothermal spheres and ellipsoids (e.g., Wang & Turner 1997; Evans & Wilkinson 1998; Keeton et al. 2000; Rhie 2010), with which the ring+point lens shares several features. In most of these models, the pseudo-caustics appear as large smooth circles or ellipses.

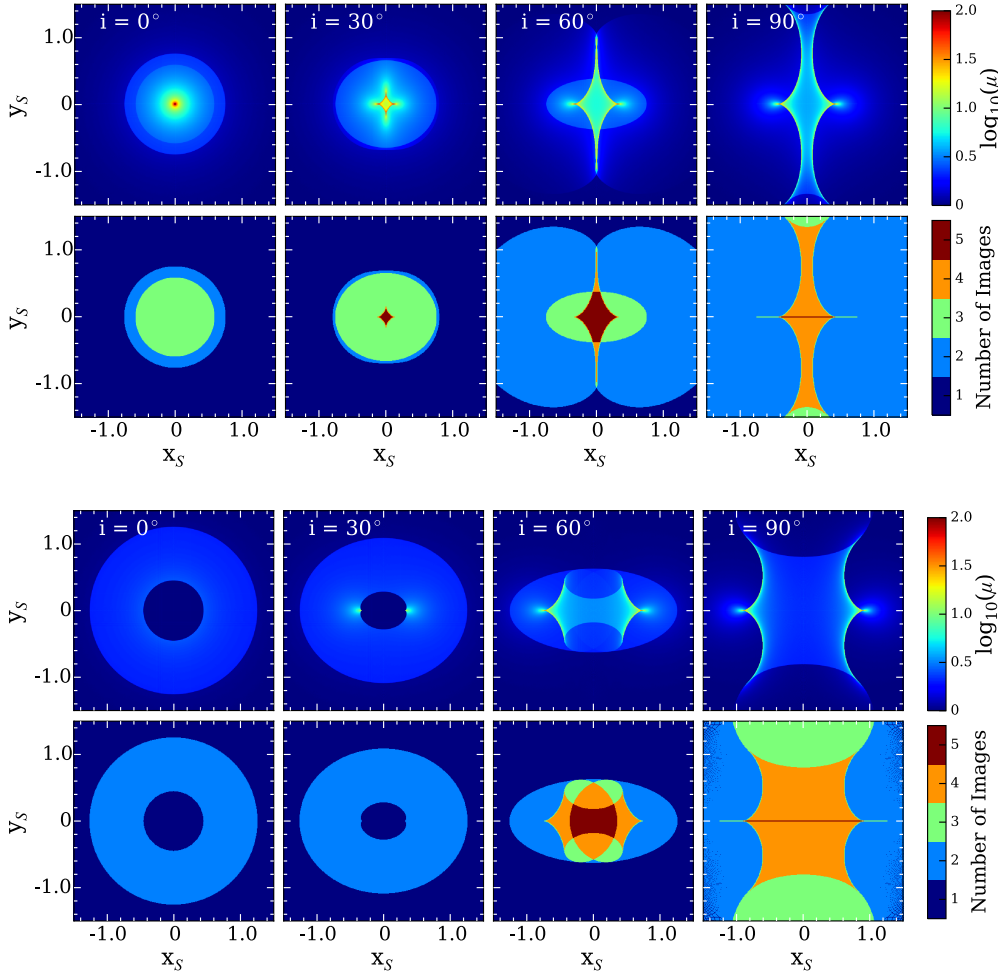


Figure 3. Magnification and image multiplicity maps for a ring-only lens. The top plot shows a ring of radius $a = 0.75$ across a range of inclinations. The top row shows the magnification μ in the source plane, with the bottom row showing the number of images a source at a given position produces. The bottom plot is the same as the upper plot, but with the ring radius changed to $a = 1.25$. Note that in both cases there are loci with finite change in magnification and with corresponding change in the number of images, which are pseudo-caustics discussed in the text.

It is tempting to attribute the presence of pseudo-caustics in the thin ring case to the discontinuity of the lensing mass distribution across the ring. However, the belt lensing systems we consider also exhibit a wide variety of pseudo-caustic features, even though the change in lensing mass is continuous across the belt. Rather, it is the non-differentiability of the deflection angle that causes the formation of the pseudo-caustics. We will show that the pseudo-caustics correspond to the boundaries of the belt/ring in the image plane mapped to the source plane. Since the lens mapping just inside or just outside of the belt/ring is continuous, each pseudo-caustic set (corresponding to the inner/outer boundary of the belt/ring) is smooth, in contrast with the (cusped) formal caustics.

Since the pseudo-caustics represent loci where the magnification map is non-differentiable, they can in principle be found by finding points in the source plane across which the magnification is discontinuous. However, an analytic formula for $\nabla\mu$ is difficult to obtain for inclined systems. In practice, with the inverse ray-shooting results, we can numerically compute the magnification map in the source plane and the associated image multiplicity map, which allow us to find the pseudo-caustics.

3.1 Ring-Only Systems

To proceed, we first turn our attention to the simplest case – that of a ring-only lensing system. Figure 3 shows magnification and image multiplicity maps for a range of ring parameters. The top plot shows a ring with radius $a = 0.75$, while in the bottom plot the ring has $a = 1.25$. In both cases, the inclination of the ring increases from left to right, going from face-on to edge-on. The top rows of each plot show magnification, while the bottom panels indicate the number of images for a source at the given location in the source plane.

In the $a = 0.75$ case (top plot), we see many boundaries between regions of different image multiplicities, where the magnification has a finite jump. These are the pseudo-caustic curves mentioned above. In the face-on case (leftmost panel), from small to large radii, we see a circular three-image region, an annular two-image region, and finally the one-image region, divided by the two pseudo-caustic curves. The feature can be understood by plotting the solutions to the lens equation in a way similar to Figures 1 and 2. There are three possible solutions, one (from $r_S = r_l$) corresponding to the undeflected light passing interior to the ring and the other two (from $r_S = r_l - 1/r_l$) corresponding to the deflection

by a central point with the same mass as the ring (exterior solutions). The physically realized solutions are determined by the ring radius. For example, at $r_S \gg 1$ only one exterior solution is physical, giving rise to the one-image region.

The solution for the three-image region has one image from rays passing interior to the ring (hence undeflected), so the region must be inside the ring, which can be used to track the inclination of the ring. Indeed, as the ring becomes more inclined, the region becomes more elliptical (top plot of Fig.3). As the ring inclines, a five-image diamond region forms near the centre and a vertical structure of increased magnification appears. Since the projected mass of the inclined ring becomes more and more concentrated toward the two ends of the major axis, the normal caustic feature exhibits some similarity to that from an equal-mass binary lensing system with the two point masses symmetrically placed on the major axis, with the positions approaching $\pm a$ as the ring becomes edge-on. That is, as the inclination increases, the caustic features mimic those of close- and intermediate-separation equal-mass binary point mass (e.g., Schneider & Weiss 1986; Liebig et al. 2015) and binary isothermal sphere (Shin & Evans 2008) lenses.

The case with $a = 1.25$ (bottom plot) is fairly different. When seen face-on, the ring is no longer concentrated enough to form multiple images near the centre. The possible physical solution to the lens equation includes that from the undeflected rays and that corresponding to the case of a point-mass lens (the one with the image outside the Einstein ring radius), with the former and latter applying to small and large radii, respectively. In between, there is an annular region where both apply, and the boundaries give the two pseudo-caustic curves. As the ring becomes inclined, this annular region pinches down about the major axis, and two folded regions of high magnification appear at the inner parts of the annulus. As the inclination continues to increase, regions with higher image multiplicities start to form. As with the $a = 0.75$ case, the normal caustics share similarities with those from an intermediate-separation equal-mass binary lens. In general, we see that the pseudo-caustics are identified with rays passing either just inside or outside the ring in the image plane.

We now turn our attention to the ring+point system and provide an illustrative understanding of the pseudo-caustics and open caustics. Finally, we present the results for the belt+point system.

3.2 Ring/Belt+Point Mass Systems

3.2.1 Ring+Point Mass System

With a point mass placed at the centre of the ring/belt, the solutions become more complex. Examining the critical curves in the image plane and the corresponding caustic curves in the source plane is helpful for us to understand the lensing properties, especially the pseudo-caustics and open caustics.

The thick black curves in Figure 4 are the critical curves (top plots) and the corresponding caustic curves (bottom plot) for the ring+point system. To understand these curves, it is useful to present the *full* sets of critical and caustic curves for the interior and exterior solutions, which are shown as the blue and red curves respectively. For the interior solution, the term “full” refers to the curves determined from the centre point mass, as if the ring did not exist. For the exterior solution, “full” means that we plainly apply the exterior solution even if the rays pass interior to the ring. Or effectively, we shrink the projected ring *confocally* to a degenerate ellipse with zero minor axis so that the exterior solution can be extended to small radii. We investigate which parts

of the critical curves are allowed to form the final critical curves (thick black) given the configuration of the system, and deduce the pseudo-caustics and open caustics. For the system shown in Figure 4, the ring and point mass have equal masses, with the ring having a radius of either $a = 0.75$ or $a = 1.25$ as labelled in the panels. The inclination of the ring increases from 30° to 90° from left to right. The scales are normalized to the Einstein ring radius of the combined ring+point system.

The “full” critical curve for the interior solution is simply a circle with radius $1/\sqrt{2}$, the Einstein ring for the centre point mass (since we normalize by the Einstein ring radius for the total ring+point mass, which is twice the point mass here). The corresponding caustic is the point at the origin. For the exterior solution, the “full” critical curve is also a circle (the Einstein ring for the total ring+point mass) for the system at face-on. As the ring becomes more inclined, its mass distribution approaches more toward a binary lens with the two equal point masses symmetrically placed on the x -axis and on the two sides of the centre point mass toward $(\pm a, 0)$. The whole system mimics the one composed of three point masses (Daněk & Heyrovský 2015). For the $a = 0.75$ case, besides a big ring-like critical curve, four small ringlet-like critical curves are formed. The big and small curves correspond to the central diamond-shaped caustic and the four planetary cusp caustics, respectively. As a whole, at high inclination, the critical and caustic curves share similarities with the close-separation triple point lensing system. For the $a = 1.25$ case, the analysis is similar and at high inclination we find the system to be similar to the intermediate- or wide-separation triple lens.

With the “full” critical and caustic curves in place for both the interior and exterior solutions, we now analyse which parts of the curves are allowed by considering the validity of the solutions. Unlike in Section 3.1 where we explain things in the source plane, we find it is more intuitive to work in the image plane, since the validity of the solutions is determined by the image position (whether it is interior or exterior to the ring) and since the projected ring is also naturally described in the image plane (a.k.a. lens plane).

The dotted black curve in each critical-curve panel of Figure 4 delineates the projected ring. For the interior solution, images outside the projected ring are not physical. Therefore the part of the critical curve outside the ring (indicated by thin blue lines) is not allowed. The allowed part becomes smaller as the ring is more inclined. The corresponding caustic is still the point at the centre in the source plane.

For the exterior solution, the situation is reversed. The part of the critical curve inside the ring (indicated by thin red lines) is not allowed. In a few cases (e.g., with $a = 0.75$ and $i = 60^\circ$), the four small ringlet-like critical curves are inside the ring and hence are not allowed, which leads to the disappearance of the planetary caustics. For the case with $a = 1.25$ and $i = 60^\circ$, the allowed part of the critical curve forms four separated arclets, as a result of the truncation imposed by the ring. They lead to four separated caustic curves, and the truncation in the critical curve makes the caustic curve become open.

Since it is the position of the ring that determines which solution is valid, the pseudo-caustics can be explained by mapping the projected ring onto the source plane, according to the interior and exterior solution, respectively. The inner (outer) boundary of the mapped ring is shown as purple (green) curves in the source plane from mapping with the interior (exterior) solution in the caustic-curve panels of Figure 4. Formal caustics can become open as they intersect the mapped ring. Since the mapping properties change discontinuously as the impact point (image) crosses the ring, the

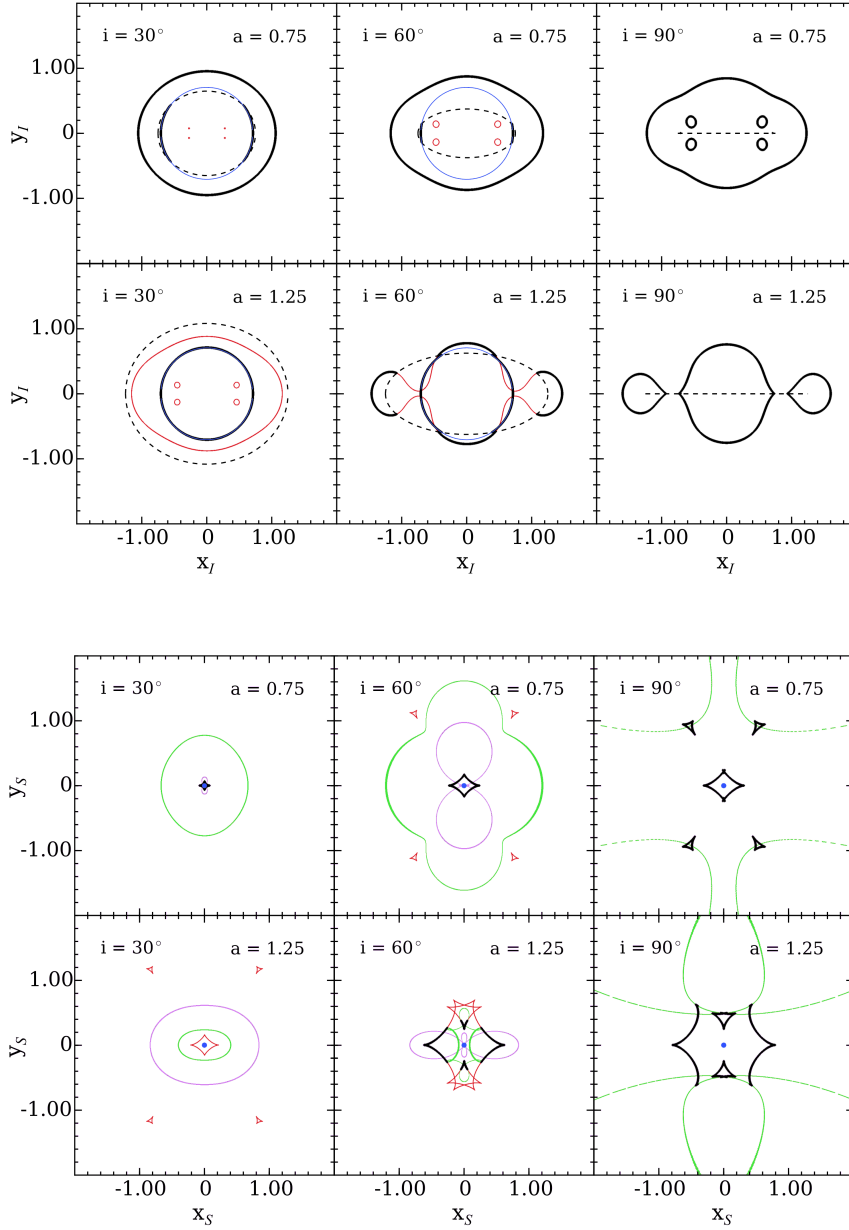


Figure 4. Critical curves (top plot) and caustic curves (bottom plot) for a ring+point lens. The ring and the point mass have equal masses. The radius and inclination of the ring are labelled in each panel. In each critical-curve panel, the blue (red) thin curves connected with the thick solid ones form the “full” critical curves from the interior (exterior) solution. The dashed curve delineates the projected ring in the image (lens) plane. The critical curves from the interior (exterior) solution becomes invalid for the parts outside (inside) the ring. The final allowed critical curves are in thick black. The corresponding caustics are denoted with the same colour and line types in the caustic-curve panels. The ring is mapped onto the source plane according to the interior (purple) and exterior (green) solution, respectively. These mapped ring curves form the pseudo-caustics. See the text for detail.

curves of the mapped ring are just the pseudo-caustics mentioned before. Notice that each pseudo-caustic is smooth, since the lens mapping is continuous just within and just outside the ring. Since the magnification is finite at the pseudo-caustics, magnification and image multiplicity maps must be constructed to study them.

Figure 5 shows the magnification and image multiplicity maps for the ring+point systems shown in Figure 4, with equal ring and point mass. Clearly, the main features in the magnification map correspond closely with the formal caustics and pseudo-caustics in Figure 4.

For $a = 0.75$ (top plot), when seen face-on, we see two pseudo-caustics (at radii ~ 0.07 and $1/\sqrt{2}$), similar to the ring-only case. However, the regions inside the pseudo-caustics have higher image multiplicities than the ring-only case. The reason is that the presence of the centre point mass allows the maximum number of solutions to be four, opposed to three as in the ring-only case. As the inclination increases, the three-image region becomes larger and more oblate. Interestingly, two lobes of *decreased* image multiplicity appear within the three-image region. When seen edge-on,

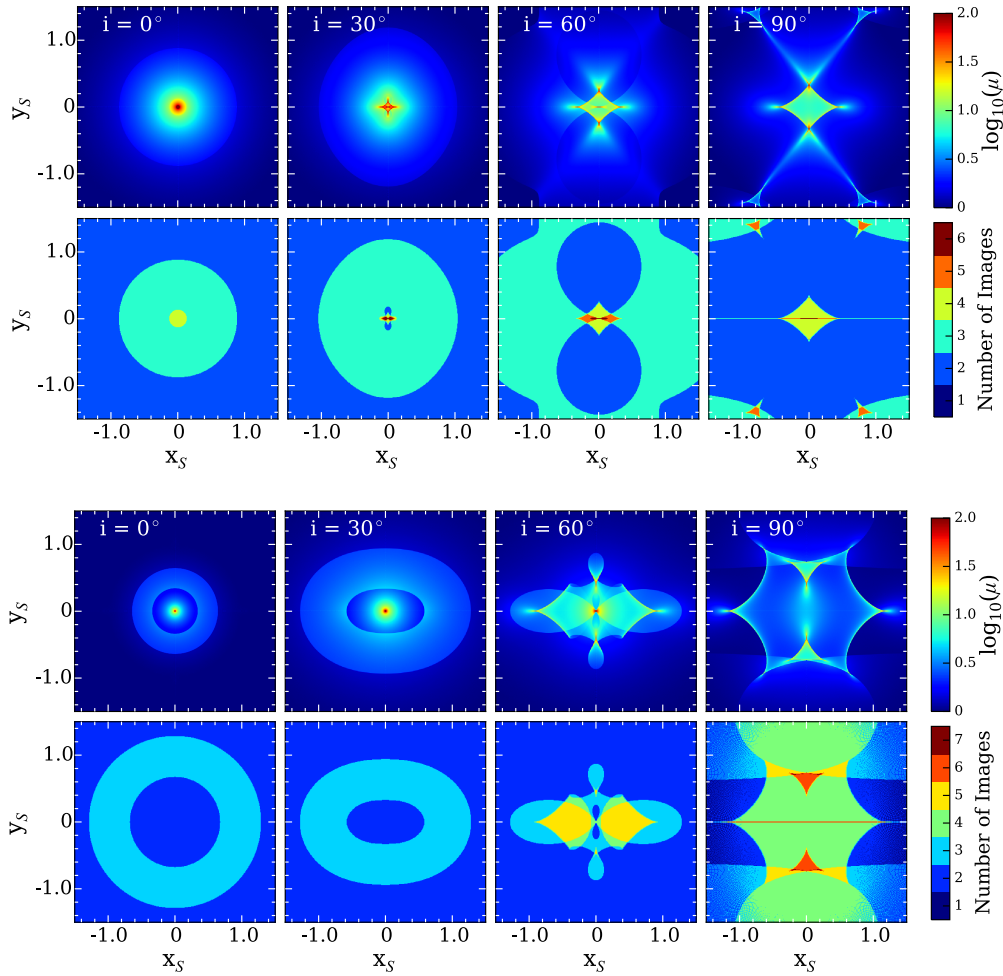


Figure 5. Magnification and image multiplicity maps for a ring+point lens. The ring and point have equal masses. The ring has radius $a = 0.75$ in the top plot and $a = 1.25$ in the bottom plot. As in Figure 3 there exist pseudo-caustics associated with changes in the image multiplicity.

these regions become larger and push out the three-image regions to larger radii.

In the bottom plot of Figure 5, the ring is enlarged to have a semi-major axis of $a = 1.25$. The pseudo-caustics in this case appear distinct from the $a = 0.75$ case. When seen face-on, we see a three-image annular region bounded by the two pseudo-caustics. When the ring inclines, the annulus folds down over itself, creating complicated overlapping features (e.g., in the panel with $i = 60^\circ$) from the interplay between the pseudo-caustics and the formal caustics. When seen edge-on, one-image regions and small seven-image regions are formed. Although edge-on $a = 0.75$ and $a = 1.25$ ring+point systems are very similar geometrically, they approximately correspond to close- and intermediate-separation triple point lensing systems and hence the magnification maps are different.

3.2.2 Belt+Point Mass System

We now widen the ring to a belt, and study the resulting effects on the morphology of the pseudo-caustics and the general magnification pattern. The lensing solutions are affected by the projected mass density (i.e., the width of the belt), as seen in Figure 1. For the following examples, we fix the belt width to be $\Delta a = 0.3$. In the belt+point case, the pseudo-caustics correspond to the inner and

outer edges of the belt mapped onto the source plane according to the interior and exterior solutions, respectively.

Figure 6 shows the magnification and image multiplicity maps for belts with different mean radii. With $\Delta a = 0.3$, the belt radius is centred at $a = 0.75$ in the top plot and $a = 1.25$ in the middle plot. In the bottom plot it is situated so that half of its mass lies outside the Einstein ring radius and half inside.

For $a = 0.75$, we only see two images formed for the face-on case, since the surface density of the belt is not high enough to generate additional images, similar to the case indicated by the blue curve in Figure 1. However, we see a ring-like structure present in the magnification map, with no correspondent image multiplicity change. This ring-like structure corresponds to rays passing through the belt, experiencing deflection from both the belt and the centre point mass. This leads to the change in the slope of the r_s - r_l relation (as illustrated in Figure 1). This means that one of the images becomes larger in size, resulting in an overall increase in magnification (dr_l^2/dr_s^2). This example shows that pseudo-caustics need not be associated with changes in the image multiplicity – they can also correspond to discontinuous changes in the size of an image.

When the belt inclines, a narrow four-image annular region bounded by pseudo-caustics appears that evolves into a fan-shaped region at $i = 60^\circ$. When the belt is seen edge-on, the magnification

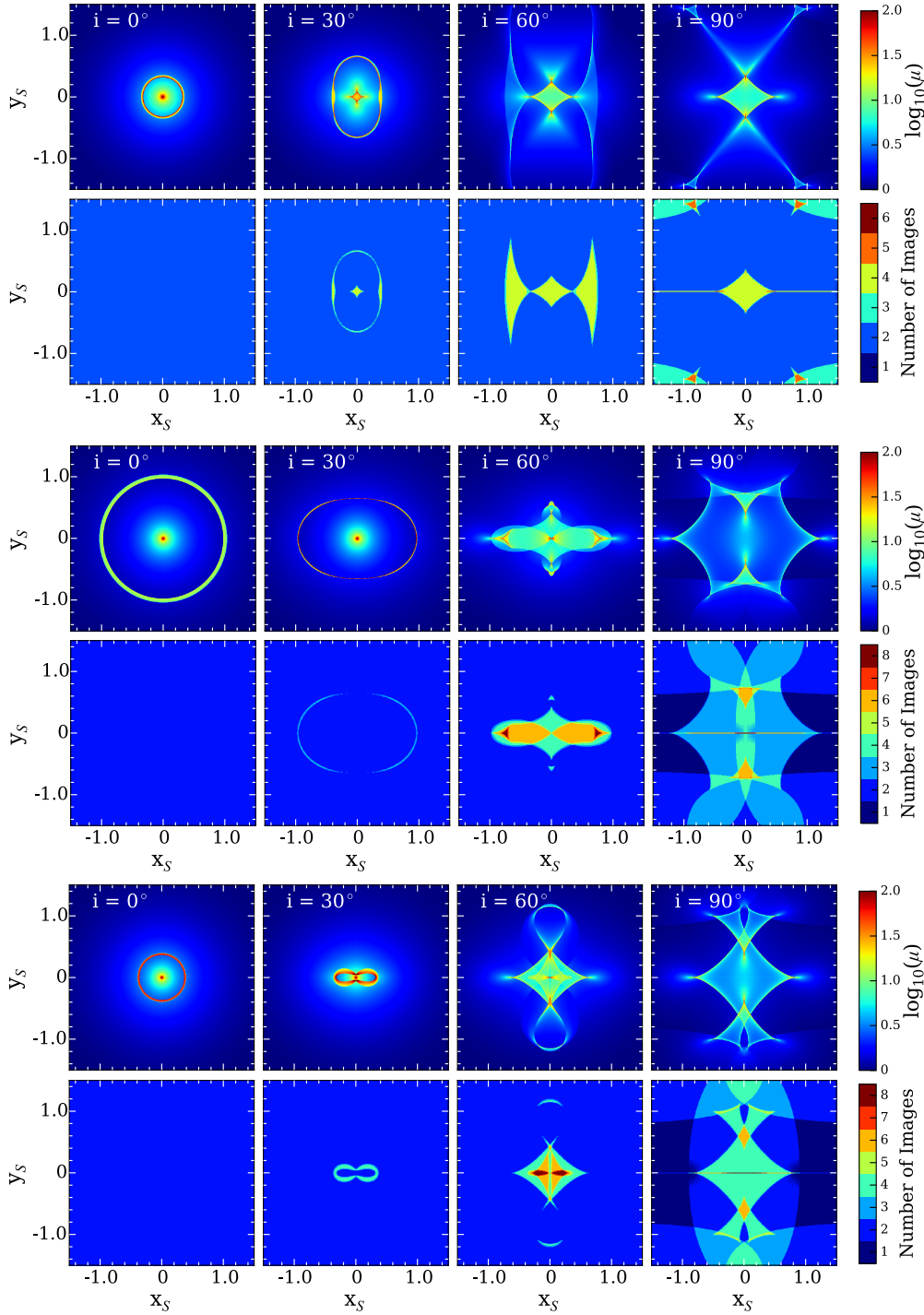


Figure 6. Magnification and image multiplicity maps for a belt+point lens at different belt inclinations. In each plot, the belt has a width of $\Delta a = 0.3$. In the top plot, the radius of the belt is centred at $a = 0.75$, in the middle plot it is centred at $a = 1.25$, and in the bottom plot the belt is situated so that half of its mass is at $a < 1$ and the other half is at $a > 1$. In all the cases, there exist pseudo-caustics associated with a discontinuous change in magnification and a corresponding change in the number or size of images.

map is similar to the case of the $a = 0.75$ edge-on ring (right panels in the top plot of Figure 5), as both approximately approach the close-separated triple point lensing system.

For the belt with radius centred at $a = 1.25$ (middle plot of Figure 6), the magnification pattern shares some broad similarities with that of the $a = 1.25$ ring case (bottom plot of Figure 5). The main noticeable differences are that at low inclination the

belt+point case has a narrower region bounded by pseudo-caustics and that in the face-on case, there is no image number change when crossing the pseudo-caustics (for the same reason as in the above $a = 0.75$ case). In particular, at edge on, the three cases from $a = 0.75$ to $a = 1.25$ are similar to the triple point lensing system going from close toward intermediate separations. The overall features for the case with half mass inside and half mass outside

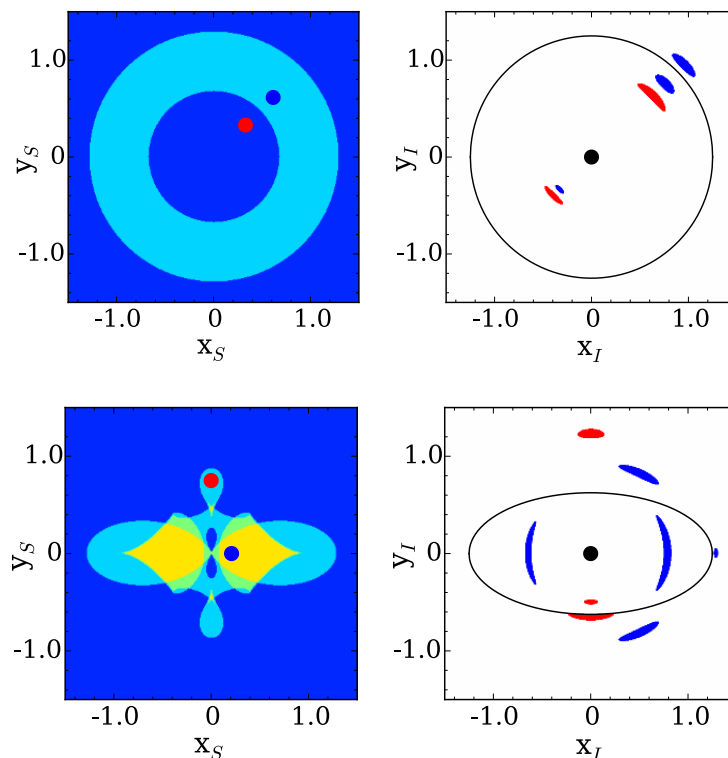


Figure 7. A demonstration of the lens mapping for two sample sources for a ring+point lens with the ring and the point having equal mass. The ring has a radius $a = 1.25$ and is seen face-on for the top panels and inclined (with inclination angle $i = 60^\circ$) for the bottom panels. The left panels show image multiplicities in the source plane, with two sources plotted as the red and blue circles. The right panels show how these sources appear in the image plane, with the ring+point system drawn in black.

the Einstein ring radius are in between the $a = 0.75$ and $a = 1.25$ cases.

3.2.3 Examples of Images from the Ring+Point System

In Figure 7, we provide examples of the sorts of images formed for sources lensed by ring+point systems. The top plot shows the case of a face-on ring with $a = 1.25$. The left panel shows the image multiplicity map with the red and blue circles representing two sources in the source plane, and the corresponding images are shown in the image plane in the right panel. The red source is mapped to two images by the centre point mass, while the blue source inside the region bounded by the pseudo-caustics is able to pass rays outside the ring (black circle) and take advantage of the ring's lensing potential to form three images, with the third appearing just outside the ring.

The bottom plot considers a slightly more complicated case, with the ring inclined to $i = 60^\circ$. Even though the image multiplicity map in the left panel looks complicated, the way in which each source is lensed is easy to understand. The red source is lensed by the centre point mass, but only one of the two possible images is inside the ring and hence is physical. The two images outside the ring come from rays deflected by both the point mass and the ring. The blue source can create two images inside the ring from deflection solely by the centre point mass. On the x_I axis, it can use additionally the ring's deflection to create an image just outside the ring. Furthermore, it can create two additional images outside the ring by taking advantage of the y_I component of the deflection. In total, five images emerge for this source.

4 SUMMARY AND DISCUSSION

In this paper, we have explored the gravitational lensing properties of a lens made of a circular ring/belt, with and without a centre point mass. The system exhibits complex features that vary with the ring/belt inclination, including open caustics and pseudo-caustics. We detail a few examples that illustrate these features.

The key property of a circular ring/belt lenses is that the rays passing interior to the projected ring/belt are not deflected by the ring/belt, while those passing exterior to the projected ring/belt are deflected. The ring/belt thus acts like a filter to select the physical solutions among possible solutions of the lens equation, which are obtained by either making its radius infinitely large (or effectively removing it) or shrinking it confocally to a point or line. Some solutions are forbidden, because they are obtained as interior solutions but correspond to rays passing exterior to the ring/belt, or vice versa. In the image (lens) plane, the ring/belt sets the boundary to determine which images are physical. Because of this selection process, for the critical curves associated with the exterior solutions, only the part exterior to the belt/ring remains, and similarly for those associated with the interior solutions. This allows for broken critical curves, and hence open caustics.

In the image plane, the ring/belt is the region that connects the interior and exterior solutions. The connection can be continuous in the belt case and discontinuous in the thin ring case. In either case, the joint solution is usually non-differentiable at the boundaries of the belt/ring. Since in general the boundaries of the belt/ring are not related to the critical curves, the boundaries are not associated with the singularities in the lensing mapping. The corresponding curves in the source plane (from mapping the belt/ring boundaries onto the

source plane) are not associated with formal caustics that have infinite magnifications, but there exists a finite discontinuity in magnification across such curves. As such, they are dubbed “pseudo-caustics”. Such a magnification change can be associated with a change in the image number (e.g., by two for a narrow belt) or not (e.g., in the case of an extended belt; see the example in Fig. 1). The magnification change in the latter case is caused by the image size change (i.e., from the change in the source-to-image mapping). Rather than a discontinuity, the magnification change can be smoothed by the continuous surface density of the belt, but we would still see an overall magnification change (a smoothed jump or a smeared pseudo-caustic) as the mapping changes, which mimics a finite-source effect. In the extreme case of a ring, the number of images can change by only one when crossing a pseudo-caustic.

The images modified by the boundaries of ring/belt in the image plane, or the magnification patterns modified by the pseudo-caustics in the source plane, form the main lensing properties of the ring/belt lens with or without centre point mass. We see the complex interplay between the ring/belt and the critical curves in the image plane or between the pseudo-caustics and the formal caustics in the source plane. Usually, analysing the caustics of a lensing system can provide enough information to figure out the image multiplicities, the general magnification patterns, and the light curve properties for a given source trajectory. However, once a ring/belt is introduced to the lensing system, in addition to the formal caustics, analysing the pseudo-caustics is needed to obtain a full picture of the lensing properties of the system. A vast amount of information hidden at finite magnifications would be missed if a study were to focus only on the formal caustics. Our work thus serves as a cautionary tale for investigations into other novel lensing geometries.

The deflection and magnification of the lens mappings we have considered can be computed analytically, and the pseudo-caustics can be easily found by mapping the edges of the ring/belt to the source plane. However, we lack an analytic expression for the image multiplicity at an arbitrary point in the source plane, which must be found numerically. A more general mathematical understanding of the connection between pseudo-caustics and image multiplicities would be of great utility to the theoretical study of gravitational lensing.

Although our analysis is mainly from a theoretical viewpoint and aims at understanding the main features in a lensing system with rings/belts, there are potential applications of our work to astronomical situations. In a related paper (Lake, Zheng, & Dong 2015), we discuss the possibility of detecting extrasolar asteroid belts based on their microlensing signatures. For the lensing system of interest, the main difference lies in the mass ratio of the belt to the centre point (star) – realistic mass ratios are around $q \sim 10^{-6}$ or smaller, as opposed to the $q = 1$ case considered here. We will show that the pseudo-caustics still have a significant effect in the magnification maps. This gives rise to interesting features in the microlensing light curve that can potentially be used to detect extrasolar asteroid belts.

5 ACKNOWLEDGEMENTS

The work is partially supported by NASA grant NNX14AC89G and NSF grant AST-1208891. The support and resources from the centre for High Performance Computing at the University of Utah are gratefully acknowledged.

REFERENCES

- Batista, V., Beaulieu, J.-P., Gould, A., et al. 2014, *ApJ*, 780, 54
 Bond, I. A., Udalski, A., Jaroszyński, M., et al. 2004, *ApJ*, 606, L155
 Bradač, M., Treu, T., Applegate, D., et al. 2009, *ApJ*, 706, 1201
 Chandrasekhar, S. 1969, *Ellipsoidal figures of equilibrium*
 Einstein, A. 1936, *Science*, 84, 506
 Erdl, H., & Schneider, P. 1993, *A&A*, 268, 453
 Lake, E., Zheng, Z., & Dong, S. B. 2015, arXiv:xxxx.xxxx
 Liebig, C., D’Ago, G., Bozza, V., & Dominik, M. 2015, *MNRAS*, 450, 1565
 Mao, S., & Paczynski, B. 1991, *ApJ*, 374, L37
 Petters, A. O., Levine, H., & Wambsganss, J. 2001, *Singularity theory and gravitational lensing*, Vol. 21 (Springer Science & Business Media)
 Rhie, S. H. 2010, *ArXiv e-prints*, arXiv:1006.0782
 Schneider, P., & Weiss, A. 1986, *A&A*, 164, 237
 Schneider, P., Ehlers, J., & Falco, E. E. 1992, *Gravitational Lenses*
 Schramm, T. 1990, *A&A*, 231, 19
 Tyson, J. A., Kochanski, G. P., & Dell’Antonio, I. P. 1998, *The Astrophysical Journal Letters*, 498, L107
 Vikram, V., Chang, C., Jain, B., et al. 2015, *ArXiv e-prints*, arXiv:1504.03002
 Wittman, D. M., Tyson, J. A., Kirkman, D., Dell’Antonio, I., & Bernstein, G. 2000, *Nature*, 405, 143
 Bourassa, R., & Kantowski, R. 1975, *ApJ*, 195, 13
 Bray, I. 1984, *MNRAS*, 208, 511
 Burke, W. L. 1981, *ApJ*, 244, L1
 Daněš, K., & Heyrovský, D. 2015, *ApJ*, 806, 99
 Evans, N. W., & Wilkinson, M. I. 1998, *MNRAS*, 296, 800
 Hoekstra, H., Bartelmann, M., Dahle, H., et al. 2013, *Space Sci. Rev.*, 177, 75
 Keeton, C. R., Mao, S., & Witt, H. J. 2000, *ApJ*, 537, 697
 Kovner, I. 1987, *ApJ*, 312, 22
 McKenzie, R. H. 1985, *Journal of Mathematical Physics*, 26, 1592
 Petters, A. O. 1995, *Journal of Mathematical Physics*, 36
 Shin, E. M., & Evans, N. W. 2008, *MNRAS*, 390, 505
 Tessore, N., & Metcalf, R. B. 2015, *A&A*, 1507.01819
 Wang, Y., & Turner, E. L. 1997, *MNRAS*, 292, 863

APPENDIX A: ANALYTIC CALCULATION OF THE MAGNIFICATION FOR THE RING/BELT+POINT SYSTEM

The magnification for a ring/belt+point system at a given point in the source plane can be obtained analytically, which is very useful for performing numerical calculations and identifying the caustic set of a given lensing geometry. The magnification at a point \mathbf{r}_I in the image plane is

$$\mu(\mathbf{r}_I) = \frac{1}{\det(A)}, \quad (\text{A1})$$

where the Jacobian of the lens mapping is given by

$$A_{ij} = \delta_{ij} - \frac{\partial \alpha_i}{\partial x_j}. \quad (\text{A2})$$

For the ring+point mass system, the Jacobian matrix is

$$A = \begin{pmatrix} 1 - g_{xx} & g_{xy} \\ g_{yx} & 1 - g_{yy} \end{pmatrix}, \quad (\text{A3})$$

where

$$\begin{aligned} g_{xx} &= \frac{1}{1+q} \frac{|\mathbf{r}_I|^2 - 2x_I^2}{|\mathbf{r}_I|^4} + \frac{q}{1+q} \frac{\partial \alpha_x}{\partial x_I} \Theta \left(\frac{x_I^2}{a^2} + \frac{y_I^2}{b^2} - 1 \right), \\ g_{xy} = g_{yx} &= -\frac{1}{1+q} \frac{2x_I y_I}{|\mathbf{r}_I|^4} + \frac{q}{1+q} \frac{\partial \alpha_x}{\partial y_I} \Theta \left(\frac{x_I^2}{a^2} + \frac{y_I^2}{b^2} - 1 \right), \\ g_{yy} &= \frac{1}{1+q} \frac{|\mathbf{r}_I|^2 - 2y_I^2}{|\mathbf{r}_I|^4} + \frac{q}{1+q} \frac{\partial \alpha_y}{\partial y_I} \Theta \left(\frac{x_I^2}{a^2} + \frac{y_I^2}{b^2} - 1 \right). \end{aligned} \quad (\text{A4})$$

The first terms in each equation are from the point mass, with the second terms coming from the ring's contribution. Here, Θ is the Heaviside step function.

The partial derivatives $\partial\alpha_i/\partial x_j$ in equation A4 can be computed analytically, yielding

$$\begin{aligned}\frac{\partial\alpha_x}{\partial x_I} &= \frac{p'^2}{a'^5 b'} \left(a'^2 - x_I \frac{\partial\lambda}{\partial x_I} \right) + \frac{2p'^4 x_I}{a'^3 b'} \left[\left(\frac{x_I^2}{a'^6} + \frac{y_I^2}{b'^6} \right) \frac{\partial\lambda}{\partial x_I} - \frac{x_I}{a'^4} \right] \\ &\quad - \frac{p'^2 x_I}{a'^4 b'^2} \frac{\partial\lambda}{\partial x_I} \left(\frac{b'}{2a'} + \frac{a'}{2b'} \right), \\ \frac{\partial\alpha_y}{\partial y_I} &= \frac{p'^2}{a' b'^5} \left(b'^2 - y_I \frac{\partial\lambda}{\partial y_I} \right) + \frac{2p'^4 y_I}{a' b'^3} \left[\left(\frac{x_I^2}{a'^6} + \frac{y_I^2}{b'^6} \right) \frac{\partial\lambda}{\partial y_I} - \frac{y_I}{b'^4} \right] \\ &\quad - \frac{p'^2 y_I}{a'^2 b'^4} \frac{\partial\lambda}{\partial y_I} \left(\frac{b'}{2a'} + \frac{a'}{2b'} \right), \\ \frac{\partial\alpha_x}{\partial y_I} &= \frac{\partial\alpha_y}{\partial x_I} = -\frac{p'^2 x_I}{a'^5 b'} \frac{\partial\lambda}{\partial y_I} + \frac{2p'^4 x_I}{a'^3 b'} \left[\left(\frac{x_I^2}{a'^6} + \frac{y_I^2}{b'^6} \right) \frac{\partial\lambda}{\partial y_I} - \frac{y_I}{b'^4} \right] \\ &\quad - \frac{p'^2 x_I}{a'^4 b'^2} \frac{\partial\lambda}{\partial y_I} \left(\frac{b'}{2a'} + \frac{a'}{2b'} \right),\end{aligned}\tag{A5}$$

where the primed variables retain their meanings from section 2.2 (see equation 12). The partial derivatives of λ are given by

$$\frac{\partial\lambda}{\partial x_I} = \frac{2p'^2 x_I}{a'^2}, \quad \frac{\partial\lambda}{\partial y_I} = \frac{2p'^2 y_I}{b'^2}.\tag{A6}$$

An analytic expression also exists for thick belts. Letting a_i and a_o be the inner and outer radii (respectively) of the belt, we compute the magnification as in (A4), but this time with the factors of $\Theta(x_I^2/a^2 + y_I^2/b^2 - 1)$ replaced by $\Theta(x_I^2/a_i^2 + y_I^2/b_i^2 - 1)$ and with

$$\begin{aligned}\frac{\partial\alpha_x}{\partial x_I} &= 2a_o b_o \left(\frac{1}{a'_o(a'_o + b'_o)} - \frac{\partial\lambda_o}{\partial x_I} \frac{x_I}{2a_o'^3 b'_o} \right) \\ &\quad - 2a_i b_i \left(\frac{1}{a'_i(a'_i + b'_i)} - \frac{\partial\lambda_i}{\partial x_I} \frac{x_I}{2a_i'^3 b'_i} \right), \\ \frac{\partial\alpha_y}{\partial y_I} &= 2a_o b_o \left(\frac{1}{b'_o(a'_o + b'_o)} - \frac{\partial\lambda_o}{\partial y_I} \frac{y_I}{2a_o' b_o'^3} \right) \\ &\quad - 2a_i b_i \left(\frac{1}{b'_i(a'_i + b'_i)} - \frac{\partial\lambda_i}{\partial y_I} \frac{y_I}{2a_i' b_i'^3} \right), \\ \frac{\partial\alpha_x}{\partial y_I} &= \frac{\partial\alpha_y}{\partial x_I} = 2a_o b_o \left(\frac{\partial\lambda_o}{\partial y_I} \frac{-x_I}{2a_o'^3 b'_o} \right) - 2a_i b_i \left(\frac{\partial\lambda_i}{\partial y_I} \frac{-x_I}{2a_i'^3 b'_i} \right),\end{aligned}\tag{A7}$$

where the primed axes are defined through

$$a_i'^2 = a_i^2 + \lambda_i, \quad b_i'^2 = b_i^2 + \lambda_i, \quad a_o'^2 = a_o^2 + \lambda_o, \quad b_o'^2 = b_o^2 + \lambda_o.\tag{A8}$$

and where

$$p'_i = \left(x_I^2/a_i'^4 + y_I^2/b_i'^4 \right)^{-1/2}, \quad p'_o = \left(x_I^2/a_o'^4 + y_I^2/b_o'^4 \right)^{-1/2}.\tag{A9}$$

As in the thin ring case, λ_i (λ_o) is found by solving equation 12 and using $a = a_i$, $b = b_i$ ($a = a_o$, $b = b_o$). The partial derivatives of λ_i are

$$\frac{\partial\lambda_i}{\partial x_I} = \frac{2p_i'^2 x_I}{a_i'^2}, \quad \frac{\partial\lambda_i}{\partial y_I} = \frac{2p_i'^2 y_I}{b_i'^2}\tag{A10}$$

while those of λ_o are

$$\frac{\partial\lambda_o}{\partial x_I} = \frac{2p_o'^2 x_I}{a_o'^2} \Theta \left(\frac{x_I^2}{a_o'^2} + \frac{y_I^2}{b_o'^2} - 1 \right), \quad \frac{\partial\lambda_o}{\partial y_I} = \frac{2p_o'^2 y_I}{b_o'^2} \Theta \left(\frac{x_I^2}{a_o'^2} + \frac{y_I^2}{b_o'^2} - 1 \right)\tag{A11}$$